

AperTO - Archivio Istituzionale Open Access dell'Università di Torino

Effect of Different Face Centered Cubic Nanoparticle Distributions on Particle Size and Surface Area Determination: A Theoretical Study

This is the author's manuscript

Original Citation:

Availability:

This version is available <http://hdl.handle.net/2318/153236> since 2015-12-07T10:41:59Z

Published version:

DOI:10.1021/jp4091014

Terms of use:

Open Access

Anyone can freely access the full text of works made available as "Open Access". Works made available under a Creative Commons license can be used according to the terms and conditions of said license. Use of all other works requires consent of the right holder (author or publisher) if not exempted from copyright protection by the applicable law.

(Article begins on next page)



UNIVERSITÀ DEGLI STUDI DI TORINO

This is an author version of the contribution published on:

Questa è la versione dell'autore dell'opera:

G. Agostini, L. Bertinetti, A. Piovano, R. Pellegrini,
G. Leofanti, E. Groppo, C. Lamberti,

“The effect of different fcc nanoparticle distributions on particle
size and surface area determination: a theoretical study”,

J. Phys. Chem. C, **118** (2014) 4085-4094

DOI: 10.1021/jp4091014

The definitive version is available at:

La versione definitiva è disponibile alla URL:

<http://pubs.acs.org/doi/abs/10.1021/jp4091014>

Effect of Different Face Centered Cubic Nanoparticle Distributions on Particle Size and Surface Area Determination: A Theoretical Study

[Giovanni Agostini](#)^{†‡*}, [Andrea Piovano](#)[§], [Luca Bertineti](#)^{||}, [Riccardo Pellegrini](#)[⊥], [Giuseppe Leofanti](#)[#], [Elena Groppo](#)[†], and [Carlo Lamberti](#)^{†∇¶}

[†] Department of Chemistry, INSTM Reference Center and NIS Centre of Excellence, Università di Torino, Via P. Giuria 7, I-10125 Torino, Italy

[‡] European Synchrotron Radiation Facility, 6 Rue Jules Horowitz, Grenoble, BP 156, F-38042, France

[§] Institut Laue-Langevin (ILL), 6 Rue Jules Horowitz, Grenoble, BP 156, F-38042, France

^{||} Department of Biomaterials, Research Campus Potsdam-Golm, Max Planck Institute of Colloids and Interfaces, 14424 Potsdam, Germany

[⊥] Catalyst Division, Chimet SpA, Via di Pesciola 74, I-52041 Viciomaggio (Arezzo), Italy

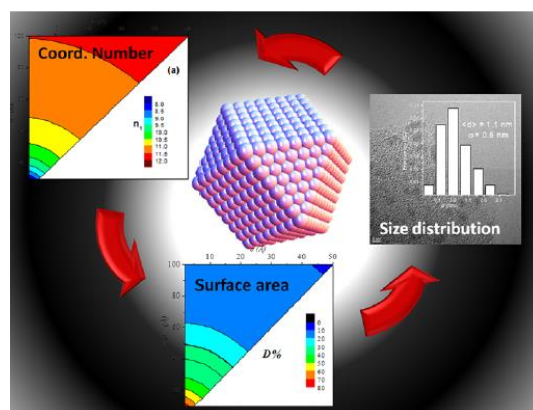
[#] Consultant, Via Firenze 43, 20010 Canegrate (Milano), Italy

[∇] CrisDI center of crystallography, University of Turin, Turin, Italy

[¶] Southern Federal University, Zorgestreet 5, 344090 Rostov-on-Don, Russia

Nanoparticles research represents one of the most active fields in science due to the importance of nanosized materials in a wide variety of applications. Their characterization needs the comparison of data coming from different experimental techniques, but the peculiar properties of the nanosystem that each technique points out are not always properly taken into account and misleading results have been often reported. In this work, we generated transmission electron microscopy like (TEM-like) data to predict the extended X-ray absorption fine structure (EXAFS) and chemisorption-like typical outputs as the average coordination numbers up to fourth shell of the particles

distribution and the surface area. The aim of the simulations is to explore the dependence of the calculated average coordination number (ACN) and average dispersion (AD) values from each parameter characterizing a particle size distribution (PSD), as the mean diameter, the width, the shape, and the profile, and shows that a range of distributions is compatible with given values of ACN and AD. In this way, we have established a general method to properly take into account the above-mentioned parameters and to allow for an accurate analysis and comparison of results. Furthermore, it will be shown that unfavorable distribution shape makes the comparison among techniques critical and potentially misleading if performed with an oversimplified model of the PSD such as those using the average diameter only.



1 Introduction

Nanoparticles research represents one of the most active fields in modern science due to the importance of nanosized materials in a wide variety of applications, such as catalysis,⁽¹⁻³⁾ photocatalysis,⁽⁴⁾ biology,^(5, 6) tunable luminescence devices, gas sensing,⁽⁷⁾ H₂ storage,⁽⁸⁾ and data storage.^(9, 10) Moreover, the role of metal nanoparticles in some highly technological applications has recently been highlighted, such as in plasmonics;⁽¹¹⁾ giant coupling effect between metal nanoparticle chain and optical waveguide; generation of electromagnetic pulses covering the terahertz (THz) gap from plasmonic silver nanoparticle arrays;⁽¹²⁾ luminescence up conversion;⁽¹³⁾ and broad band absorbing antennas.⁽¹⁴⁾

Among the different techniques available to exploit the structure of these nanosystems, transmission electron microscopy (TEM), extended X-ray absorption fine structure (EXAFS), and chemisorptions are the most widely used, especially in combination among them (see Table 1). High-resolution TEM is a powerful atomic scale technique for metal nanoparticles characterization that provides at the same time morphological and crystallographic information such as the size and shape of the nanoparticles, the crystallographic phase, arrangement of atoms in the specimen, and their degree of order.⁽¹⁵⁾ Furthermore, the distribution of the particle size can be obtained by counting all particles present on a suitable set of micrographs. This is one of the great advantages of TEM, as the output is not just a simple average number (such as with EXAFS or chemisorption) but a complete definition of the particle size distribution: mean value ($\langle d \rangle$), standard deviation (σ), and the profile of distribution.⁽¹⁶⁾

Table 1. Summary of the Main Advantages and Disadvantages of TEM, EXAFS, and Chemisorption for Particle Size Determination

technique	extracted information	detection method	single particle weight	technique limits	sensitivity	analysis limits
TEM	$\{d_i\}$	direct	1	$i < 1000$	low detection small d_i^b	treatment of aggregates
EXAFS	$\langle N_i(\{d\}) \rangle^a$	indirect	$d_i^3 / \sum_{i=1} d_i^c$	$\langle d_i \rangle$	single absorber	model dependent
chemisorption	$\langle D(\{d\}) \rangle$	indirect	$d_i^3 / \sum_{i=1} d_i$	$\langle d \rangle$	single adsorbed molecule	ξ dependent, support interaction

^a d can change as a function of particle shape. ^bLower detection limit depends strongly on metal/support contrast. ^cValid for a cluster with a single type of element.

Advantages are however accompanied by two main drawbacks: (i) the price to pay for any high-resolution imaging technique is related to the relatively small fraction of particles sampled; (ii) the lower particle/background contrast that small particles have with respect to big ones. This implies that a fraction of small particles, below 1–1.5 nm in diameter d (depending on the particle/support electron density contrast and on the instrument), could escape detection resulting in an underestimation of the small-size side of the measured particle distribution. This limitation is significantly reduced (but not completely removed) by the new generation of aberration corrected scanning transmission electron microscopes^(5, 17-20) and by working with a high-angle annular dark field detector,⁽²¹⁾ but their high cost make these facilities hardly available for systematic studies on particle size determination.

EXAFS spectroscopy probes the local environment of a selected element (the metal one in this case) providing average structural information around it. This technique analyzes the oscillations of the X-ray absorption coefficient caused by the interference between the outgoing and incoming photoelectron waves that depends on the distance between absorber and scattering atoms and on their atomic numbers. Consequently the fine structure of the spectra contains information about the atomic environment of absorbing atoms in terms of the number and type of neighbors, interatomic distance, and structural disorder.⁽²²⁾ The atomic selectivity and the short-range sensitivity make EXAFS a powerful tool for the nanoparticles characterization.^(1, 16, 23-40) Finally, a large fraction of material can be sampled, making EXAFS statistically reliable.

Starting from the coordination number of the first shell and with a hypothesis about the morphology of the clusters, it is possible to correlate the average coordination number (ACN) with the size of the nanoparticles analyzed. Moreover, it has been demonstrated that, including in the data analysis the entire set of the first four coordination numbers, EXAFS can provide morphological information.^(29-31, 33) Also in this case two main drawbacks have to be considered: (i) EXAFS provides only the average of the coordination numbers, without any information about the broadening of the particle size distribution (PSD) or possible distribution inhomogeneity; (ii) EXAFS is unable to discriminate particles from bulk metal, when $\langle d \rangle$ exceeds a critical value of $\sim 4\text{--}5$ nm.

Chemisorption of molecule A is the measure of the number N_A of molecules adsorbed on the surface of a well-known amount of sample at a given temperature and pressure.[\(41, 42\)](#) For a large case of supported metal catalysts (Pd, Pt, and Au, etc.) carbon monoxide is the most used probe for chemisorption experiments. From the mean stoichiometry of the adsorbed molecule–surface atoms adduct it is possible to extract the number of surface atoms of the sample. The final output of a chemisorption experiment is the metal dispersion D , defined as the fraction of surface atoms, over the total number of metal atoms ($N_{\text{metal_tot}}$). This technique is very powerful for nanoparticles characterization as it allows detection of all surface metal atoms accessible to the probe molecule, independently of the particle size. Furthermore, a large fraction of material can be sampled, being so statistically reliable.

Three main limits are however present: (i) chemisorption provides only average information,[\(43\)](#) (ii) particles with $\langle d \rangle$ higher than $\sim 4\text{--}5$ nm are unnoticeable to metal bulk; (iii) the D value can be extracted from the measured values N_A and $N_{\text{metal_tot}}$ only once the surface stoichiometry ratio ξ has been assumed: $D = \xi (N_A/N_{\text{metal_tot}})$. Formally, the ξ value depends not only on the sample temperature but also on the nature of the metal and the (hkl) indexes of the exposed metal face. In fact, the ability of molecule A to form linear, 2- or 3-fold bridged adducts depends on the surface arrangements of the metal atoms.[\(44-48\)](#) It is worth noticing that even for the largely investigated case of carbon monoxide adsorbed at room temperature on Pd metal particles, the spread of the measured or assumed ξ values in literature is still impressive, ranging from 0.5 to 1.[\(16, 44, 49-54\)](#) Finally, it should be mentioned that the D value represents an underestimation of the actual dispersion as it does not account for the fraction of the surface inaccessible to probe A because in interaction with the support or because of surface poisoning.[\(50\)](#)

The average particle size $\langle d \rangle$ can be directly measured by TEM or, once a particle morphology is assumed, they can also be indirectly deduced from both the ACN obtained from EXAFS N or from the average dispersion AD measured by chemisorption.[\(16, 55\)](#) However it is fundamental to properly weight the contribution of each single nanoparticle to the total signal for every technique to achieve a correct comparison of the results. In TEM analysis the particle size distribution is determined by weighting each nanoparticle in the same way independently of its size. On the contrary, in EXAFS and chemisorption, the relative weight of a single nanoparticle to the total signal is represented by its volume fraction with respect to the total volume of all of the particles of the distribution (vide infra eq [3](#)).

Taking into account the relative advantages and drawbacks of TEM, EXAFS, and chemisorption (Table [1](#)), it is evident that a great benefit can be obtained by combining the three techniques. Nevertheless, the goal of this work is to underline that the results coming from these three techniques cannot be easily compared and sophisticated methods have to be adopted to achieve the correct quantitative results. We propose a general method for the interpretation and comparison of shape and cluster sizes from different techniques for a cluster with any size and different reasonable shapes. The very simple hypotheses adopted, i.e., perfect clusters with face centered cubic structure, allowed us to focus on ideal populations of particles without any other particular prerequisite.

For further information we emphasize that to determine ACN and AD additional techniques available are small-Angle X-ray scattering (SAXS)[\(56-59\)](#) and Pair Distribution Function (PDF) from the total scattering data, respectively.[\(60-62\)](#) These techniques are much less widespread among the scientific community in comparison with TEM, EXAFS, and chemisorption, and for this reason in this work we will not enter in details about their advantages and drawbacks.

The discussion is structured so that the reader can face step by step the progressive rise of the number of variables and thus the complexity up to the final global simulation procedure. First simulations with a well-defined size and different cluster shape will be treated. Then, fixed to a particular shape, the influence of distribution type will be presented, followed by the study of the

importance of the distribution asymmetry and distribution homogeneity (bimodal distributions). These parameters influence significantly the results as demonstrated hereafter.

2 Methods: Algorithm Description

The algorithm developed to calculate the dispersion AD and the ACN up to the fourth shell (N_1 , N_2 , N_3 , and N_4) for a given particles size distribution consists of two successive steps. As the first step, a discrete particle size distribution $\{d_1, d_2, \dots, d_n \equiv \{d_i\}$ consisting of n particles with a well-defined mean value ($\langle d \rangle$), standard deviation (σ), and profile (i.e., Gaussian, Lognormal, Multimodal) is generated by a Monte Carlo method. Note that the distribution $\{d_i\}$ obtained is independent of the cluster shape and in the following, when not explicitly declared, a Gaussian particle distribution $\{d_i\}$ has been used. From $\{d_i\}$, the dispersion D and coordination numbers (N_1 , N_2 , N_3 and N_4) of the distribution are then calculated as follows:

$$D = \sum_i^n D(d_i) w(d_i) \quad (1)$$

$$N_j = \sum_i^n N_j(d_i) w(d_i) \quad (j = 1, 2, 3, 4) \quad (2)$$

Equations 1 and 2 consist of the sum on all n particles of the distribution of its corresponding N_j or D multiplied by the weight $w(d_i)$.

The values of the $N_j(d_i)$ and $D(d_i)$ functions are defined for each particle shape and shell order while the weight-function $w(d_i)$ is the volume fraction of a single particle of diameter d_i respect the total volume of all particles of the distribution $\{d_i\}$:

$$w(d_i) = \frac{1}{V_{\text{TOT}}} \frac{4}{3} \pi \left(\frac{d_i}{2} \right)^3 \quad \text{with } V_{\text{TOT}} = \sum_i^n \frac{4}{3} \pi \left(\frac{d_i}{2} \right)^3 \quad (3)$$

The algorithm allows to have thorough grasp of the parameters of the simulation both on the shape of cluster and on the mean, standard deviation values and profile of the distribution.

3 Results and discussion

3.1 Effect of the Particle Shape: Ideal Case with $\sigma = 0$

The first parameter we consider, that significantly affects the $\langle d \rangle$ calculated from TEM, EXAFS, and chemisorption data, is the cluster shape. Consequently, to isolate its effect, distributions with standard deviation equal to zero have been considered.

In literature many types of regular polyhedral shapes have been proposed for metal clusters.[\(63-70\)](#) In this work, three of them have been chosen due to their particular relevance: cuboctahedral (**CO**), icosahedral (**ICO**), and truncated cuboctahedral (**TCO**) shapes. **CO** is a widely adopted cluster shape when modeling metal nanoparticles with face centered cubic structure and it is obtained by truncating the lattice along $\{100\}$ and $\{111\}$ directions. **ICO** is an interesting shape as it is obtained by distortion of a **CO**.[\(71\)](#) **TCO** is usually observed when the metal nanoparticles interact strongly with the support and it comes from cuboctahedrons cut along the (111) plane going cross the diameter of clusters.

Following the method proposed by Montejano-Carrizales et al.[\(55\)](#) we considered only perfect crystals built adding one by one complete layers of atoms around the central one; in this way, three series of clusters with different shapes (for **CO**, **ICO** and **TCO**) and dimensions have been obtained. For all *fcc* metals, the number of layers added is indicated by letter “*m*”[\(55\)](#) and relationship between the number m of layers and cluster dimension changes as a function of the lattice parameter and it is defined by the equation:

$$d(m) = 1.173am + 2R_{cov} \quad (4)$$

where a is the cell parameter and R_{cov} the covalent radius of the chemical element considered. It is worth noticing that, although our analytical method does not put any constrain in particle size, the empirical construction method using eq 4 does not allow to obtain particles with less than a complete shell around central atom, i.e. $d(1) = 7.18 \text{ \AA}$ in the case of Pd. Nevertheless, below this limit it is not possible to define a real shape as there is not a unique complete shell of atoms which could be arranged in a precise way.

The dispersion of the clusters decreases with the particle diameter and it is the same for all cluster shapes. This assertion is certainly correct for **CO** and **ICO** clusters because the distortion of the *fcc* lattice does not affect the ratio of surface and total atoms of **ICO**(55, 71) but in principle it is wrong for **TCO**. In fact **TCO** is obtained cutting **CO** along its diameter, in this way the number of surface atoms with respect to the total increases and consequently the dispersion changes. But supported **TCO** particles are the consequence of a strong interaction with the support along their (111) plane(72-74) making so the new generated face unavailable for chemisorption. Consequently supported **TCO** particles exhibit 1/2 of both total and surface available atoms of the **CO** particle of same d , and exhibit consequently the same D . The analytical expression of dispersion as a function of the order m was proposed by Montejano-Carrizales et al.(55) and holds for **CO**, **ICO** and **TCO** shapes.

More complicated is to obtain the coordination numbers N_j : analytical expressions are available only for the first shell of **CO** and **ICO**,(55) but for the aim of this study this is not sufficient and a database of the coordination numbers for higher shells and for the three cluster shape is needed. The values for N_1 , N_2 , N_3 and N_4 have been calculated in this work, for the three shapes (**CO**, **ICO** and **TCO**), for m values up to 10, interpolated with analytical polynomial function for non integer m values and converted into d using eq 4. Obtained values are reported in Figure 1 as a function of both m and d for the palladium case ($a = 3.889 \text{ \AA}$). These values agree with the analytical values of N_1 ,(55) and with analogous data reported in literature for the higher shells by Glasner and Frenkel.(75)

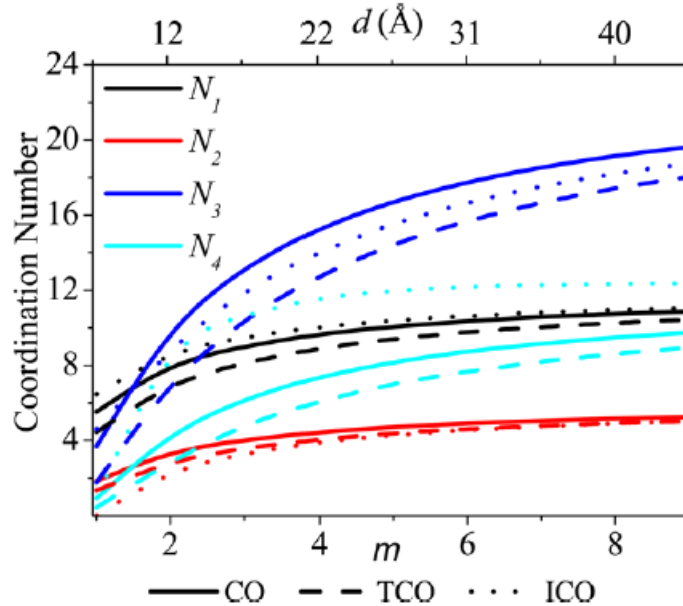


Figure 1. Comparison of the average coordination numbers of the first 4th shells for cluster with different shapes: cuboctahedron (**CO**), truncated cuboctahedron (**TCO**) and, icosahedrons (**ICO**), solid, dashed, and dotted lines respectively. The data are plotted in terms of order m (bottom abscissa axes) and of the particles diameter in case of Pd nanoparticles (top abscissa axes) with cell parameter 3.889 \AA and shortest distance Pd–Pd 2.75 \AA .(76)

The data reported in Figure 1 highlight that the coordination numbers not only depends on the size and shape of clusters but they are univocally correlated to both dimension and shape. This is in agreement with previous works of Frenkel et al.(30, 31)

From Figure 1, it emerges that for the first and second shells, N_1 and N_2 values are very similar for all shapes and that once error bars are taken into account, it will be almost impossible to discriminate between different shapes from experimental data analyzed only up to the second shell. Starting from the third shell the coordination numbers begin to differ each other in a more significant way and it becomes consequently possible to extract a three-dimensional information able to distinguish between **CO**, **ICO** and **TCO** clusters from a complete analysis of high-quality EXAFS data.(30, 31, 33)

3.2 Beyond the $\sigma = 0$ Approximation: Correlation among $\langle d \rangle$, σ , N_j , D

The approach adopted in the previous paragraph, considering distributions with $\sigma = 0$, is useful to underline the relationships between the size and shape of clusters and the shell order but a real particle size distribution is always characterized by a spread of particles dimensions. A series of Gaussian particles size distributions of **CO** have been generated changing $\langle d \rangle$ in the range 10–100 Å, and standard deviation σ in the range 2–50 Å. For each of them, the dispersion D and the coordination numbers N_j have been calculated according to eqs 1 and 2 and the results have been reported in Figure 2 and Figure 3, respectively.

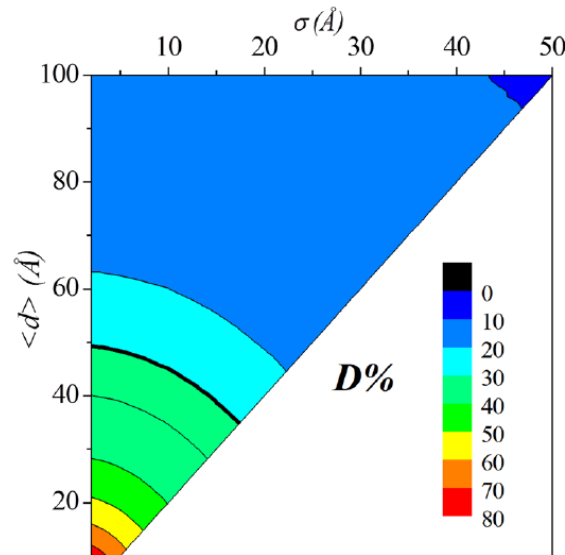


Figure 2. Metal nanoparticles dispersion as a function of $\langle d \rangle$ and σ for Gaussian particle distributions of nanoparticles with cuboctahedral shape. The intervals adopted are 10–100 Å for $\langle d \rangle$ and 2–50 Å for σ . Particles dimensions are referred to Pd nanoparticle with cell parameter 3.889 Å and shortest distance Pd–Pd 2.75 Å. (76) Image has been cut at a meaningful value of $2\sigma = \langle d \rangle$. Meaningful information limit has been arbitrarily fixed to the 85% of bulk value, highlighted by the bold black line.

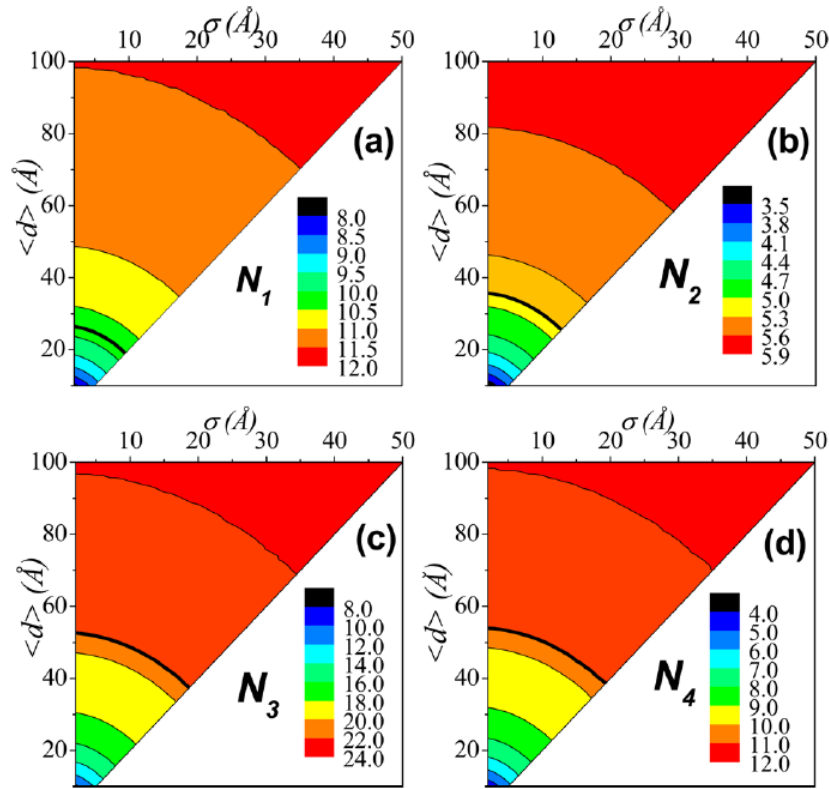


Figure 3. Average coordination number as a function of the mean and standard deviation values for Gaussian particle distributions and clusters with cuboctahedral shape: effect on first (a), second (b), third (c), and fourth (d) shell coordination number N_j . Particle dimensions are referred to Pd nanoparticle with cell parameter 3.889 Å and shortest distance Pd–Pd 2.75 Å.⁽⁷⁶⁾ Images have been cut at a meaningful value of $2\sigma = \langle d \rangle$. Meaningful information limit has been arbitrarily fixed to the 85% of bulk value, highlighted by the bold black line in each inset.

All data demonstrate that D and N_j depend not only on the $\langle d \rangle$ value but also on the σ value of distributions. This fact implies that while an experimental PSD obtained by TEM or by SAXS can be used to estimate D and N_j values obtained by chemisorption and EXAFS, the reverse process (estimating $\langle d \rangle$ from EXAFS or chemisorption data) is not a straightforward process, as it is usually assumed in the literature.

Indeed, both D and N_j are informative only for small particles and narrow distributions because, with an increase in the average particle size and/or with broader distributions, the slope of $D(\langle d \rangle, \sigma)$ and $N_j(\langle d \rangle, \sigma)$ surfaces (shown in Figure 2 and Figure 3) decreases making unreliable the extraction of any information from chemisorptions and EXAFS data. As far as D is concerned, the meaningful information limit could be arbitrarily fixed to 85% of bulk value that is highlighted by the bold black line in Figure 2. Below this line the profile of the $D(\langle d \rangle, \sigma)$ surface is too flat to allow a reliable discrimination among all possible different cases resulting to the same D value with its associated experimental incertitude. More complex is the situation for the coordination numbers since the slope of the surface changes as a function of the shell order as already observed in Figure 1 in the case of $\sigma = 0$. Applying the same arbitrary criterion of 85% of bulk value, the information limits are 10.2, 5.1, 19.2, and 10.2 for N_1 , N_2 , N_3 , and N_4 , respectively. Observing the position of bold black lines in Figure 3a–d, it emerges that the higher shells are informative for distributions with larger mean and standard deviation values with respect to the first one.

It is important to note that, for both D and N_j , the lower the $\langle d \rangle$, the greater the influence of σ in determining the D and N_j values. This is extremely relevant when a comparison among data collected with different techniques (TEM, EXAFS, and chemisorption) is attempted. With the exception of a few works (see e. g., refs. 16, 50, and 77), the large majority of literature reporting a combined TEM/EXAFS or TEM/chemisorption study uses only the $\langle d \rangle$ value obtained from TEM

to correlate the average particle diameter obtained from the different techniques, neglecting σ . In the light of what has been discussed above, it is clear that this simplified approach induces a systematic error in the comparison. This error can be quantified as follows:

$$\Delta D/\% = \frac{D(\langle d \rangle, \sigma) - D(\langle d \rangle, \sigma = 0)}{D(\langle d \rangle, \sigma = 0)} \quad (5)$$

$$\Delta N_j/\% = \frac{N_j(\langle d \rangle, \sigma) - N_j(\langle d \rangle, \sigma = 0)}{N_j(\langle d \rangle, \sigma = 0)} \quad (6)$$

For each point of the surfaces shown in Figure 2 and Figure 3, eqs 5 and 6 have been applied and the results are reported in Figure 4 and Figure 5 for D and N_j , respectively. For a better comprehension, data are plotted in two dimensions as a function of σ : curves with the same color indicate distributions with the same $\langle d \rangle$ value.

The first observation is that the errors are always negative for D (overestimation of D) and positive for N_j (underestimation of N_j). In fact, small particles are characterized by high dispersion and, if errors calculated by (5) are negative, it means that $D(\langle d \rangle, \sigma=0) > D(\langle d \rangle, \sigma)$. Therefore, without considering the σ , for the same mean d value higher dispersions are obtained. In this way, when experimental data of dispersion are associated with particle dimensions, the mean d value results higher than the real diameter. The same stands for N_j , but in this case small particles have low N_j : positive errors calculated by (6) correspond to $N_j(\langle d \rangle, \sigma = 0) < N_j(\langle d \rangle, \sigma)$, and therefore the calculated particles size is larger than the real size averaged over the distribution. In other words, when EXAFS or chemisorption data are used to estimate $\langle d \rangle$ of an unknown distribution $\{d_i\}$, the estimated value is always larger than the real one: the larger the σ of the real distribution, the larger the error. This point is of particular relevance, as EXAFS or chemisorption data alone are unable to estimate the value of σ .

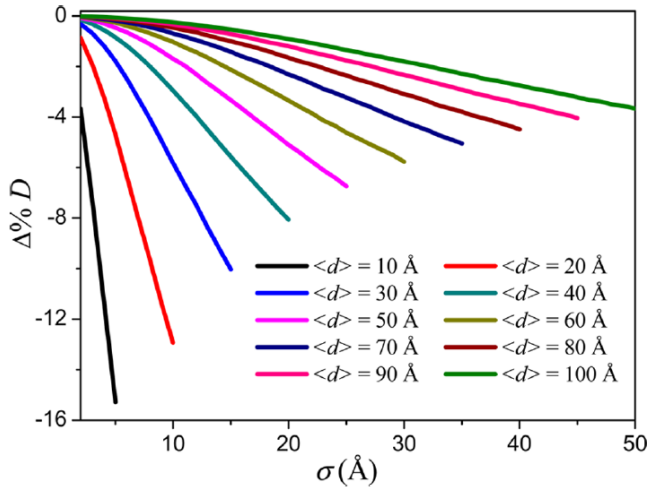


Figure 4. Systematic error in the evaluation of the dispersion D , eq 6, plotted as a function of σ . The different curves correspond to distributions $\{d_i\}$ with different mean values $\langle d \rangle$ in the 10–100 Å range. Particle dimension is referred to Pd nanoparticle with cell parameter 3.889 Å and shortest distance Pd–Pd 2.75 Å.⁽⁷⁶⁾ Curves were cut at a meaningful value of $2\sigma = \langle d \rangle$.

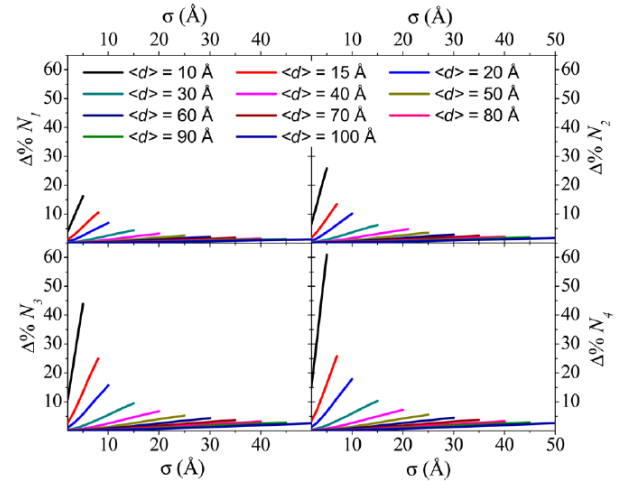


Figure 5. Systematic error in the evaluation of the coordination numbers of the first four shells N_j , eq 6, plotted as a function of σ . The different curves correspond to $\{d_i\}$ with different $\langle d \rangle$ in the 10–100 Å range. Particle dimension is referred to Pd nanoparticle with cell parameter 3.889 Å and shortest distance Pd–Pd 2.75 Å.⁽⁷⁶⁾ Curves were cut at a meaningful value of $2\sigma = \langle d \rangle$.

More in details, D is strongly affected by σ , in fact the errors are negligible only for narrow distribution and high mean values. This assertion is clear when observing the slopes of the lines in

Figure 4 that increase quickly with σ . Furthermore, for small particle sizes the condition limit $2\sigma = \langle d \rangle$ is rapidly reached. As for the coordination numbers, the influence of σ is more pronounced for the higher shells (smaller values of the critical σ): the slope of the curves for the same $\langle d \rangle$ in Figure 5 increases with the shell order.

In the light of results just obtained, it is clear that understanding the role of σ in determining D and N_j values of a $\{d_i\}$ is of utmost importance. The next aspect to explore is then the different weight of particle with different dimension in the determination of D and N_j of a particle size distribution. A correct comparison of chemisorption or EXAFS results with the particle size distribution obtained by TEM measurement can be performed only once N_j and D are weighted following eq 3. This is because, in the comparison, it is not relevant the fraction of particles with a particular diameter, but their contribution to the total volume of the particle size distribution. This concept and the related consequences are more clear by looking at Figure 6, where the blue histogram represents a well-defined particle size distribution characterized by $\langle d \rangle = 20$ Å and $\sigma = 5$ Å, while the red histogram represents the distribution obtained by multiplying each single diameter class fraction for its volume and normalizing with respect to the total volume. It is evident that, for the latter distribution, the highest column of volume distribution occurs for higher values than the $\langle d \rangle$ (represented by black line), reflecting the heavier role played by particles with larger diameter. More than 86% of the volume is hosted on the right side of $\langle d \rangle$. This datum is not surprising considering that $\langle d \rangle$ is the result of a simple arithmetic average while the volume is proportional to d^3 .

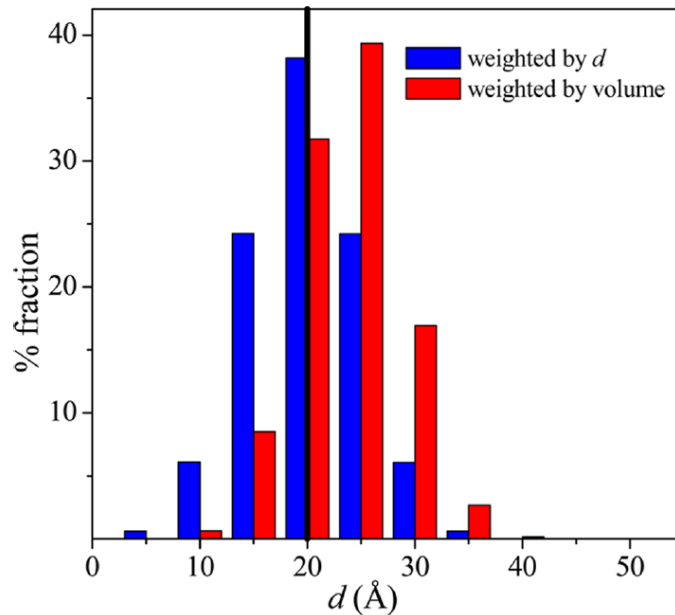


Figure 6. Gaussian particle size distribution with $\langle d \rangle = 20$ and $\sigma = 5$ Å (blue histogram) and the corresponding particle volume distribution computed by weighting each i th particle by eq 3 (red histogram). The vertical black line represents the average particle size distribution ($d = 20$ Å). In the case of the red histogram, the particles on the right side of the $\langle d \rangle$ value correspond to 86% of the total volume

The different role played by small and big particles of a distribution $\{d_i\}$ to D and N_j values is the origin of the error done using only the $\langle d \rangle$ value of the distribution and neglecting σ .

3.3 Symmetrical vs Asymmetrical Particle Size Distributions (Gaussian vs Log-Normal)

Not even $\langle d \rangle$ and σ are parameters sufficient to characterize a PSD when D and N_j have been extracted. In fact, starting from two distributions with exactly the same mean and standard deviation values but different profile, Gaussian and log-normal by blue and red columns of Figure 7, D and N_j have been calculated. The results have been reported in the second and third columns of Table 2

together with the percentage difference between the two cases. D moves from 50 to 45% with a difference of $\Delta D/\% = 10$, while considering coordination numbers the difference is small for the first shell, only 3%, but it increases with the shell order up to 15% in the fourth one. The importance of the profile of the size distribution increases with the shell order.

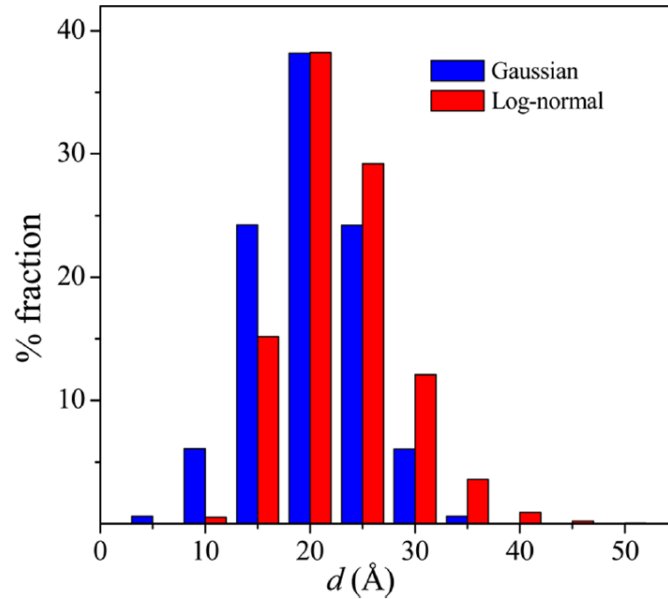


Figure 7. Particle size distribution with the same $\langle d \rangle = 20$ and $\sigma = 5$ Å, but different shape: Gaussian distribution (blue histogram) and log-normal distribution (red histogram).

Table 2. Dispersion and Coordination Numbers up to Fourth Shell Computed for Gaussian and Log-Normal Distributions $\{d_i\}$ with $\langle d \rangle = 20$ Å $\sigma = 5$ Å (see Figure 7)^a

	Gaussian distribution	log-normal distribution	$\Delta D/\%$
D , %	50	45	+10
N_1	9.0	9.3	-3
N_2	4.0	4.2	-5
N_3	13.3	14.2	-7
N_4	6.0	6.9	-15

^aAlso the percentage difference is reported in the last column.

3.4 Bimodal Particle Distribution: Homogeneity of Nanoparticles Population

The study of dispersion and coordination number becomes more complex when the nanoparticles population is constituted by bimodal distributions. In these cases an accurate TEM analysis is fundamental to determine precisely the particle size distribution allowing the correct interpretation of EXAFS and chemisorption measurements that provides only average values of N_j and D .

Very critical for a bimodal distribution is the case of inhomogeneity, i.e., when only a few percent of particles with larger diameter are present in the sample. To clarify this point N_j and D of a monomodal Gaussian distribution (with $\langle d \rangle = 20$ Å and $\sigma = 5$ Å) have been calculated and compared with a population obtained starting from the previous one and adding 5% of cluster with $d = 50$ Å. The two distributions are reported in Figure 8, while the quantitative results are reported in Table 3.

The results reported in Table 3 indicate that the inhomogeneity of the sample strongly affects both N_j and D . D moves from 50% to 40% resulting in $|\Delta D| = 20\%$, while with regard to coordination numbers this is relevant especially for the higher shells: the difference reaches 30% for the fourth shell but already for the first one, 9%, it is not negligible

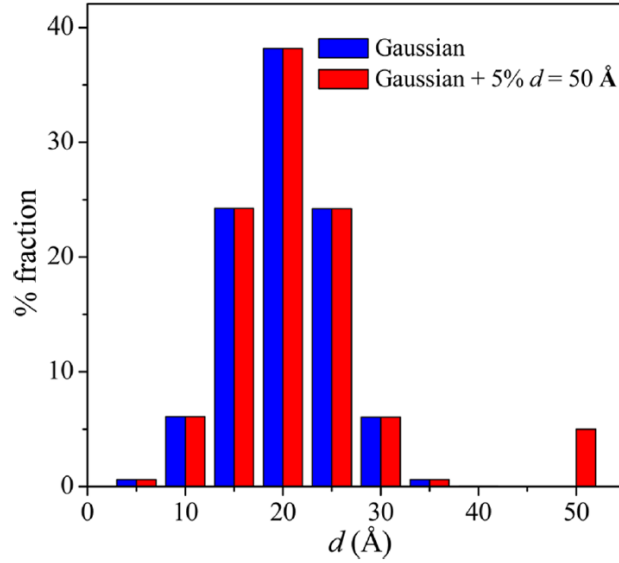


Figure 8. Particle size distribution with Gaussian profile characterized by $\langle d \rangle = 20$ and $\sigma = 5$ Å (blue histogram) and same distribution with 5% of particles with $d = 50$ Å added (red histogram).

Table 3. Dispersion and Coordination Numbers up to the Fourth Shell Computed for Gaussian Distribution ($\langle d \rangle = 20$ Å and $\sigma = 5$ Å) and for a Distribution Obtained by Adding to the First One 5% of Nanoparticles with $d = 50$ Å (See Figure 8)

	Gaussian	Gaussian + 5% $d = 50$ Å	$\Delta\%$
$D, \%$	50	40	+20
N_1	9.0	9.8	-9
N_2	4.0	4.5	-12
N_3	13.3	15.9	-20
N_4	6.0	7.8	-30

3.5 Cumulative Effects

Until now we have examined, on both N_j and D , the effect of (i) a nonnull σ ; (ii) a nonsymmetrical diameter distribution profile (Gaussian vs log-normal distributions), and (iii) the presence of a bimodal distribution. These three cases have been considered separately, but they may be simultaneously present in a real $\{d_i\}$. The values of D and N_j for each distribution up to now presented are reported in Table 4 together with the maximum percentage error committed in neglecting the different distribution variables.

Comparing the results reported in Table 4, the differences considering only $\langle d \rangle$ and all error sources are impressive. D falls from 54 to 38% with a percentage difference of 30%. In the EXAFS data already for the first shell, that is, the shell less affected by error sources, the N_1 changes from 8.6 to 9.8 with a percentage difference of 14%. For the highest shell, N_4 increases from 5.7 to 7.8 resulting in a difference as large as 37%.

3.6 Inverse Problem

Until now, we have assumed well-defined theoretical (generated by MC simulation) or experimental (measured by TEM or SAXS) particle size distributions from which we have computed the resulting first four shells coordination numbers N_j and the dispersion D . Now we will discuss the difficulties in studying the inverse problem: i.e., the estimation of both $\langle d \rangle$ and σ once the cluster shape has been assumed knowing N_1 , N_2 , N_3 , and N_4 , and possibly D .

It has already been demonstrated by Frenkel et al.,[\(29-31\)](#) and Witkowska et al.[\(33\)](#) that once N_1 , N_2 , N_3 , and N_4 are known, the dimension and the shape of the cluster (**CO**, **TCO**, or **ICO**) can be univocally determined. This conclusion is true for a distribution with $\sigma = 0$, but on the basis of what has been discussed so far, it emerges that in cases where $\sigma \neq 0$ (i.e., in all real cases) this conclusion is subordinated to the $\langle d \rangle$ and σ values and to the experimental errors associated with N_1 , N_2 , N_3 , N_4 , and D .

Table 4. Dispersion and Coordination Numbers up to Fourth Shell Computed for (i) an Ideal Distribution with $\langle d \rangle = 20$ Å and $\sigma = 0$ Å; (ii) a Gaussian Distribution with $\langle d \rangle = 20$ Å and $\sigma = 5$ Å; (iii) a Log-Normal (log N) Distribution with $\langle d \rangle = 20$ Å and $\sigma = 5$ Å; and (iv) a Bimodal Distribution $\{d_i\} = 1.00\{d_i^a\} + 0.05\{d_i^b\}$ being $\{d_i^a\}$ a Log-Normal distribution with $\langle d \rangle = 20$ Å and $\sigma = 5$ Å and $\{d_i^b\}$ Distribution with $\langle d \rangle = 50$ Å and $\sigma = 0$ Å^a

	$\sigma = 0$	$\sigma = 5$ Å			
		Gaussian	log N	log $N + 5\%d = 50$ Å	max $\Delta\%$
D	54	50	45	38	30
N_1	8.6	9.0	9.3	9.8	14
N_2	3.7	4.0	4.2	4.5	22
N_3	12.1	13.4	14.2	16.0	32
N_4	5.7	6.4	6.9	7.8	37

^a The value 0.95 is from ref [2](#). For comparison, the difference in percentage (max $\Delta\%$) among the first ($\sigma = 0$) and the fourth (log $N + 5\%d = 50$ Å) case is also reported [max $\Delta\% = ((\text{col } 2) - (\text{col } 5))/(\text{col } 5)$].

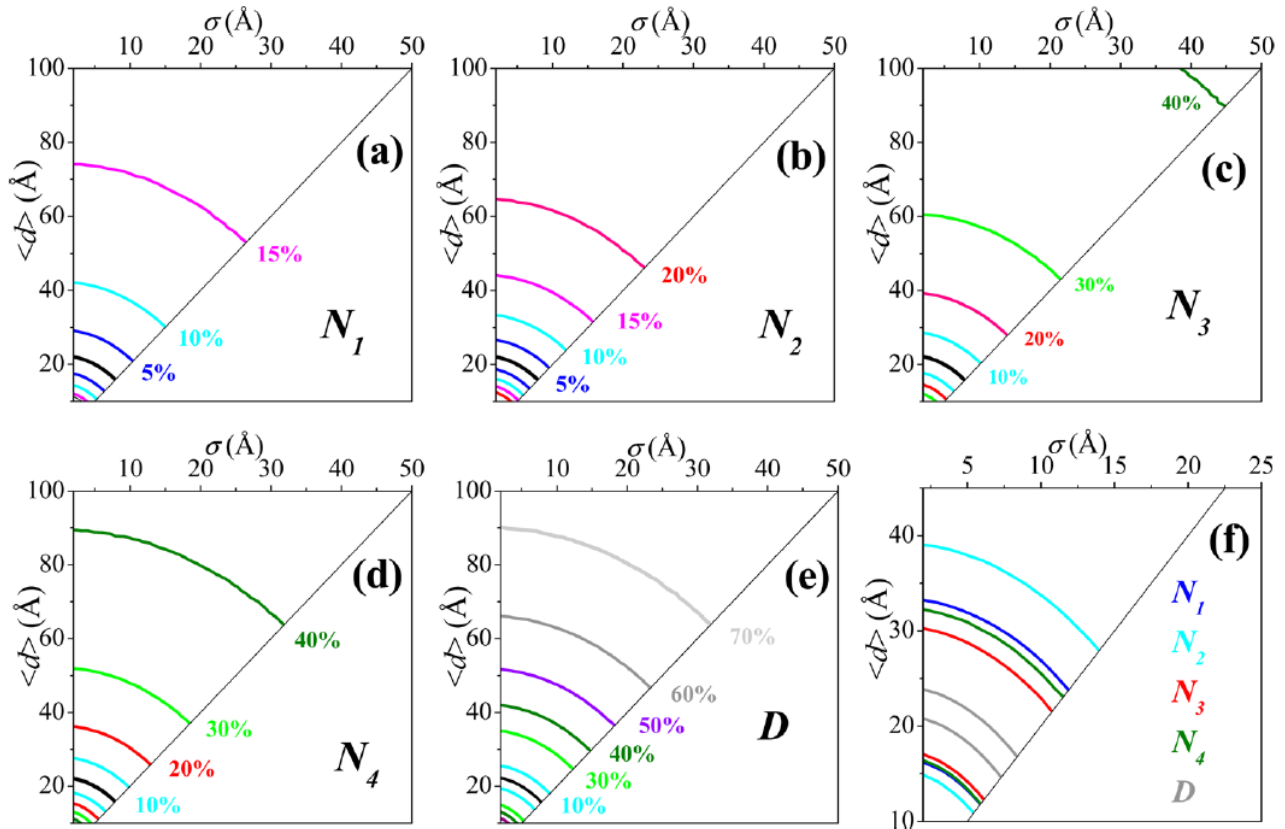


Figure 9. (a–e) black curves, couples of $\langle d \rangle$ and σ values compatible with coordination numbers of $N_1 = 9.0$, $N_2 = 4.0$, $N_3 = 13.4$, and $N_4 = 6.4$ and with a dispersion of $D = 50\%$; color curves, the intervals of the $\langle d \rangle$ – σ plane compatible with the values reported above, assuming different relative errors. (f) Intervals of the $\langle d \rangle$ – σ plane for the same N_j and D compatible with the typical experimental errors from high-quality EXAFS and chemisorption data collection and analysis, i.e., 7%, 13%, 12%, and 17%, as well as 5% for N_1 , N_2 , N_3 , and N_4 , as well as D , respectively. For all parts, the **CO** shape has been assumed and particle dimension is referred to Pd nanoparticle with cell parameter 3.889 Å and shortest distance Pd–Pd 2.75 Å.[\(76\)](#) Curves were cut at a meaningful value of $2\sigma = \langle d \rangle$.

Assuming a Gaussian particle size distribution of particle with CO shape and neglecting σ , the values $N_1 = 9.0$, $N_2 = 4.0$, $N_3 = 13.4$, $N_4 = 6.4$ and $D = 0.50$ correspond to particle dimension $\langle d \rangle = 22.5$ Å. However, removing the constraint $\sigma = 0$ Å, infinitely different $\langle d \rangle$ and σ values are compatible with the five numbers reported above because a decrease in $\langle d \rangle$ can be compensated for by an increase in σ . All possible values lie on the black curves reported in Figure 9a–e; among them are the following: ($\langle d \rangle = 20$ Å, $\sigma = 5$ Å); ($\langle d \rangle = 17$ Å, $\sigma = 7$ Å); ($\langle d \rangle = 15$ Å, $\sigma = 9$ Å); ($\langle d \rangle = 13$ Å, $\sigma = 10$ Å); ($\langle d \rangle = 10$ Å, $\sigma = 11$ Å); ($\langle d \rangle = 7$ Å, $\sigma = 12.5$ Å). Only measuring or assuming σ an univocal value for $\langle d \rangle$ can be obtained, even from coordination numbers and dispersion values ideally non affected by experimental errors.

When N_j and D values are obtained by EXAFS and chemisorption experiments, mean values are associated with corresponding errors. Typical error bars for good quality EXAFS data collected on metal nanoparticles of comparable size distribution and refined by experts(33) are as follows: $\Delta N_1 = \pm 0.8$ ($\pm 7\%$), $\Delta N_2 = \pm 0.8$ ($\pm 13\%$), $\Delta N_3 = \pm 3$ ($\pm 12\%$), and $\Delta N_4 = \pm 2$ ($\pm 17\%$). Coming to chemisorption data, from our experience(1, 16, 50) we know that the reproducibility of the data repeated on the same sample batch is $\pm 0.5\%$. However, this error does not include systematic errors such as the correct average metal/molecule surface stoichiometry, the assumption on the particle shape, or the fraction of particle in interaction with the support. A more reliable evaluation is consequently $\Delta D = \pm 5\%$.

Parts a–e of Figure 9 report how the experimental errors of increasing values associated with N_j and D propagate in the determination of $\langle d \rangle$ and σ . From the inspection of the incertitude regions, it is evident that for whatever associated error the higher coordination shells allow a more precise determination of the $\langle d \rangle$ and σ values, defining a smaller region in the $\langle d \rangle$ – σ plane. For the same relative errors an even better result is obtained from the dispersion datum.

The data reported in Figure 9f show the same curves together assuming the typical error associated with each variable: 7, 13, 12, and 17, as well as 5% for N_1 , N_2 , N_3 , and N_4 , as well as D , respectively. The best accuracy is obtained, by far, from D , for both the lower impact of error propagation and the lower intrinsic experimental error. Among the different values extracted from the EXAFS data analysis, the better accuracy is reached by N_3 ; testing the importance to analyze the trend in the particle size determination among different shells from the better to the worse is N_3 , N_4 , N_1 , and N_2 .

However, chemisorption provides a single number, which in relation to $\langle d \rangle$ and σ values is based on several assumptions that need to be carefully verified case by case to avoid systematic errors of much larger amplitude. An example is reported by Pellegrini et al.(50) where the fall of the dispersion of doped 2 wt % Pd on SiO₂–Al₂O₃ samples in the absence of other experimental data could be misinterpreted as an impressive particle sintering instead of the actual covering of the metal nanoparticle by an amorphous phase. This latter interpretation of the chemisorption data was demonstrated by coupling chemisorption with EXAFS and TEM investigations.

4 Conclusion

In this work we dealt with an intrinsically highly difficult problem in the field of analysis methods for materials characterization. We showed that EXAFS and chemisorption provide only average information on nanoparticles and alternative hypotheses are necessary for the data interpretation. On the contrary, TEM is a very powerful technique because it is a direct investigation method, but the reliability of measurements is a critical point both for the low statistics and for detection limit of small nanoparticles. To overcome these drawbacks and to obtain a complete and reliable characterization, a complementary techniques approach is mandatory, and in this work we explored the correct method to combine them.

Once a theoretical (obtained by Monte Carlo approach) or an experimental (obtained by TEM or SAXS) particle size distribution has been obtained, the correct approach to estimate the D and N_j

values is proposed in eqs 1 and 2, which takes into account the whole distribution. Starting from simulations, it has been demonstrated that the dispersion and the average coordination numbers for the first, second, third, and fourth coordination shells of a face centered cubic metal nanoparticles distribution strongly depend on the mean value, standard deviation, and profile of the particle size distribution. Moreover, it has been shown that the most critical point in the metal nanoparticles characterization, both for surface area and particle size determination, is the homogeneity of the sample investigated because a little fraction of larger particles provides significant difference in the final results. Oversimplified approaches, where only $\langle d \rangle$ is considered or narrow distributions with large mean values, are biased by relevant systematic errors.

In conclusion, the determination of N_1 , N_2 , N_3 , and N_4 values from EXAFS and/or of D from chemisorption does not allow one to obtain independently $\langle d \rangle$ and σ , even neglecting the experimental incertitude, but provides only couples of $\langle d \rangle$ – σ values. Once the experimental incertitude is considered, then a region of the $\langle d \rangle$ – σ plane is defined, the D parameter being the most efficient one in limiting the extension of this region, although based on several assumptions that needs to be carefully verified case by case. With regard to coordination numbers more accurate results have been obtained by higher shells, justifying the great effort made in the data analysis with respect to a simple first shell determination.

The authors declare no competing financial interest.

Acknowledgment

This work has been supported by “Progetti di Ricerca di Ateneo-Compagnia di San Paolo-2011-Linea 1A, ORTO11RRT5 project”.

References

- (1) Agostini, G.; Groppo, E.; Piovano, A.; Pellegrini, R.; Leofanti, G.; Lamberti, C. Preparation of Supported Pd Catalysts: From the Pd Precursor Solution to the Deposited Pd^{2+} Phase. *Langmuir* 2010, 26, 11204–11211.
- (2) Dotzauer, D. M.; Dai, J. H.; Sun, L.; Bruening, M. L. Catalytic membranes prepared using layer-by-layer adsorption of polyelectrolyte/ metal nanoparticle films in porous supports. *Nano Lett.* 2006, 6, 2268–2272.
- (3) Park, J. Y.; Zhang, Y.; Grass, M.; Zhang, T.; Somorjai, G. A. Tuning of catalytic CO oxidation by changing composition of Rh–Pt bimetallic nanoparticles. *Nano Lett.* 2008, 8, 673–677.
- (4) Su, R.; Tiruvalam, R.; He, Q.; Dimitratos, N.; Kesavan, L.; Hammond, C.; Lopez-Sanchez, J. A.; Bechstein, R.; Kiely, C. J.; Hutchings, G. J.; Besenbacher, F. Promotion of Phenol Photodecomposition over TiO_2 Using Au, Pd, and Au–Pd Nanoparticles. *ACS Nano* 2012, 6, 6284–6292.
- (5) Wang, Z. D.; Zhang, J. Q.; Ekman, J. M.; Kenis, P. J. A.; Lu, Y. DNA-Mediated Control of Metal Nanoparticle Shape: One-Pot Synthesis and Cellular Uptake of Highly Stable and Functional Gold Nanoflowers. *Nano Lett.* 2010, 10, 1886–1891.
- (6) Willner, I.; Willner, B. Biomolecule-Based Nanomaterials and Nanostructures. *Nano Lett.* 2010, 10, 3805–3815.
- (7) Zanolli, Z.; Leghrib, R.; Felten, A.; Pireaux, J. J.; Llobet, E.; Charlier, J. C. Gas Sensing with Au-Decorated Carbon Nanotubes. *ACS Nano* 2011, 5, 4592–4599.
- (8) Langhammer, C.; Zoric, I.; Kasemo, B. Hydrogen storage in Pd nanodisks characterized with a novel nanoplasmonic sensing scheme. *Nano Lett.* 2007, 7, 3122–3127.
- (9) Lu, A.-H.; Salabas, E. L.; Schueth, F. Magnetic nanoparticles: Synthesis, protection, functionalization, and application. *Angew. Chem., Int. Ed.* 2007, 46, 1222–1244.
- (10) Reiss, G.; Hutten, A. Magnetic nanoparticles-Applications beyond data storage. *Nat. Mater.* 2005, 4, 725–726.
- (11) Halas, N. J. Plasmonics: An Emerging Field Fostered by Nano Letters. *Nano Lett.* 2010, 10, 3816–3822.
- (12) Polyushkin, D. K.; Hendry, E.; Stone, E. K.; Barnes, W. L. THz Generation from Plasmonic Nanoparticle Arrays. *Nano Lett.* 2011, 11, 4718–4724.
- (13) Saboktakin, M.; Ye, X. C.; Oh, S. J.; Hong, S. H.; Fafarman, A. T.; Chettiar, U. K.; Engheta, N.; Murray, C. B.; Kagan, C. R. Metal- Enhanced Upconversion Luminescence Tunable through Metal Nanoparticle-Nanophosphor Separation. *ACS Nano* 2012, 6, 8758–8766.

- (14) Carmeli, I.; Lieberman, I.; Kravinsky, L.; Fan, Z. Y.; Govorov, A. O.; Markovich, G.; Richter, S. Broad Band Enhancement of Light Absorption in Photosystem I by Metal Nanoparticle Antennas. *Nano Lett.* 2010, 10, 2069–2074.
- (15) Williams, D. B.; Carter, C. B., *Transmission Electron Microscopy: A Textbook for Materials Science*, 2nd ed.; Springer: Berlin, 2009.
- (16) Agostini, G.; Pellegrini, R.; Leofanti, G.; Bertinetti, L.; Bertarione, S.; Groppo, E.; Zecchina, A.; Lamberti, C. Determination of the Particle Size, Available Surface Area, and Nature of Exposed Sites for Silica-Alumina-Supported Pd Nanoparticles: A Multitechnical Approach. *J. Phys. Chem. C* 2009, 113, 10485–10492.
- (17) Muller, D. A.; Kourkoutis, L. F.; Murfitt, M.; Song, J. H.; Hwang, H. Y.; Silcox, J.; Dellby, N.; Krivanek, O. L. Atomic-scale chemical imaging of composition and bonding by aberration-corrected microscopy. *Science* 2008, 319, 1073–1076.
- (18) Uzun, A.; Ortalan, V.; Hao, Y. L.; Browning, N. D.; Gates, B. C. Nanoclusters of Gold on a High-Area Support: Almost Uniform Nanoclusters Imaged by Scanning Transmission Electron Microscopy. *ACS Nano* 2009, 3, 3691–3695.
- (19) Aydin, C.; Lu, J.; Liang, A. J.; Chen, C. Y.; Browning, N. D.; Gates, B. C. Tracking Iridium Atoms with Electron Microscopy: First Steps of Metal Nanocluster Formation in One-Dimensional Zeolite Channels. *Nano Lett.* 2011, 11, 5537–5541.
- (20) Lopez-Haro, M.; Cies, J. M.; Trasobares, S.; Perez-Omil, J. A.; Delgado, J. J.; Bernal, S.; Bayle-Guillemaud, P.; Stephan, O.; Yoshida, K.; Boyes, E. D.; Gai, P. L.; Calvino, J. J. Imaging Nanostructural Modifications Induced by Electronic Metal-Support Interaction Effects at Au Parallel to Cerium-Based Oxide Nanointerfaces. *ACS Nano* 2012, 6, 6812–6820.
- (21) Rebled, J. M.; Yedra, L.; Estrade, S.; Portillo, J.; Peiro, F. A new approach for 3D reconstruction from bright field TEM imaging: Beam precession assisted electron tomography. *Ultramicroscopy* 2011, 111, 1504–1511.
- (22) Filipponi, A.; Di Cicco, A. X-ray-absorption spectroscopy and n-body distribution functions in condensed matter 0.2. Data analysis and applications. *Phys. Rev. B* 1995, 52, 15135–15149.
- (23) Bordiga, S.; Groppo, E.; Agostini, G.; van Bokhoven, J. A.; Lamberti, C. Reactivity of Surface Species in Heterogeneous Catalysts Probed by in Situ X-ray Absorption Techniques. *Chem. Rev.* 2013, 113, 1736–1850.
- (24) Mino, L.; Agostini, G.; Borfecchia, E.; Gianolio, D.; Piovano, A.; Gallo, E.; Lamberti, C. Low-dimensional systems investigated by X-ray absorption spectroscopy: A selection of 2D, 1D and 0D cases. *J. Phys. D: Appl. Phys.* 2013, 46.
- (25) Kip, B. J.; Duivenvoorden, F. B. M.; Koningsberger, D. C.; Prins, R. Determination of Metal-Particle Size of Highly Dispersed Rh, Ir, and Pt Catalysts by Hydrogen Chemisorption and EXAFS. *J. Catal.* 1987, 105, 26–38.
- (26) Koningsberger, D. C.; Mojet, B. L.; van Dorssen, G. E.; Ramaker, D. E. XAFS spectroscopy; fundamental principles and data analysis. *Top. Catal.* 2000, 10, 143–155.
- (27) Pinto, A.; Pennisi, A. R.; Faraci, G.; Dagostino, G.; Mobilio, S.; Boscherini, F. Evidence for Truncated Octahedral Structures in Supported Gold Clusters. *Phys. Rev. B* 1995, 51, 5315–5321.
- (28) Boscherini, F.; de Panfilis, S.; Weissmuller, J. Determination of local structure in nanophase palladium by X-ray-absorption spectroscopy. *Phys. Rev. B* 1998, 57, 3365–3374.
- (29) Frenkel, A. I. Solving the structure of nanoparticles by multiplescattering EXAFS analysis. *J. Synchrotron Radiat.* 1999, 6, 293–295.
- (30) Frenkel, A. I.; Hills, C. W.; Nuzzo, R. G. A view from the inside: Complexity in the atomic scale ordering of supported metal nanoparticles. *J. Phys. Chem. B* 2001, 105, 12689–12703.
- (31) Frenkel, A. Solving the 3D structure of metal nanoparticles. *Z. Kristallogr.* 2007, 222, 605–611.
- (32) Russell, A. E.; Rose, A. X-ray absorption spectroscopy of low temperature fuel cell catalysts. *Chem. Rev.* 2004, 104, 4613–4635.
- (33) Witkowska, A.; Di Cicco, A.; Principi, E. Local ordering of nanostructured Pt probed by multiple-scattering XAFS. *Phys. Rev. B* 2007, 76, No. 104110.
- (34) Agostini, G.; Usseglio, S.; Groppo, E.; Uddin, M. J.; Prestipino, C.; Bordiga, S.; Zecchina, A.; Solari, P. L.; Lamberti, C. From Isolated Ag⁺ Ions to Aggregated Ag⁰ Nanoclusters in Silver-Exchanged Engelhard Titanosilicate (ETS-10) Molecular Sieve: Reversible Behavior. *Chem. Mater.* 2009, 21, 1343–1353.
- (35) Groppo, E.; Liu, W.; Zavorotynska, O.; Agostini, G.; Spoto, G.; Bordiga, S.; Lamberti, C.; Zecchina, A. Subnanometric Pd Particles Stabilized Inside Highly Cross-Linked Polymeric Supports. *Chem. Mater.* 2010, 22, 2297–2308.
- (36) Guzman, J.; Gates, B. C. Gold nanoclusters supported on MgO: Synthesis, characterization, and evidence of Au(6). *Nano Lett.* 2001, 1, 689–692.

- (37) Alayoglu, S.; Zavalij, P.; Eichhorn, B.; Wang, Q.; Frenkel, A. I.; Chupas, P. Structural and Architectural Evaluation of Bimetallic Nanoparticles: A Case Study of Pt–Ru Core-Shell and Alloy Nanoparticles. *ACS Nano* 2009, 3, 3127–3137.
- (38) Allard, L. F.; Panjabi, G. A.; Salvi, S. N.; Gates, B. C. Imaging of nearly uniform Os₅C clusters dispersed on MgO powder. *Nano Lett.* 2002, 2, 381–384.
- (39) Lai, F. S.; Gates, B. C. Nanoclusters of iridium oxide and of rhodium oxide supported on MgO. *Nano Lett.* 2001, 1, 583–587.
- (40) Coker, V. S.; Bennett, J. A.; Telling, N. D.; Henkel, T.; Charnock, J. M.; van der Laan, G.; Patrick, R. A. D.; Pearce, C. I.; Cutting, R. S.; Shannon, I. J.; Wood, J.; Arenholz, E.; Lyon, I. C.; Lloyd, J. R. Microbial Engineering of Nanoheterostructures: Biological Synthesis of a Magnetically Recoverable Palladium Nanocatalyst. *ACS Nano* 2010, 4, 2577–2584.
- (41) Anderson, J. R.; Pratt, K. C. Surface area measurement. *Introduction to Characterization and Testing of Catalysts*; Academic Press: New York, 1986; pp 1–53.
- (42) Lemaitre, J. L.; Menon, P. G.; Delannay, F. The Measurement of Catalyst Dispersion. In *Characterization of Heterogeneous Catalysts*; Delannay, F., Ed.; Marcel Dekker: New York, 1984; Vol. 15, pp 299–365.
- (43) Pellegrini, R. Synthesis, characterization and activity of Pd supported nanoparticles for hydrogenation reactions. Ph.D. Thesis, University of Torino, Italy, 2008.
- (44) Stara, I.; Nehasil, V.; Matolin, V. Influence of substrate structure on activity of alumina supported Pd particles: CO adsorption and oxidation. *Surf. Sci.* 1996, 365, 69–77.
- (45) Henry, C. R. Surface studies of supported model catalysts. *Surf. Sci. Rep.* 1998, 31, 235–325.
- (46) Ozensoy, E.; Goodman, D. W. Vibrational spectroscopic studies on CO adsorption, NO adsorption CO plus NO reaction on Pd model catalysts. *Phys. Chem. Chem. Phys.* 2004, 6, 3765–3778.
- (47) Groppo, E.; Bertarione, S.; Rotunno, F.; Agostini, G.; Scarano, D.; Pellegrini, R.; Leofanti, G.; Zecchina, A.; Lamberti, C. Role of the support in determining the vibrational properties of carbonyls formed on Pd supported on SiO₂–Al₂O₃, Al₂O₃, and MgO. *J. Phys. Chem. C* 2007, 111, 7021–7028.
- (48) Lamberti, C.; Zecchina, A.; Groppo, E.; Bordiga, S. Probing the surfaces of heterogeneous catalysts by in situ IR spectroscopy. *Chem. Soc. Rev.* 2010, 39, 4951–5001.
- (49) Prelazzi, G.; Cerboni, M.; Leofanti, G. Comparison of H₂ Adsorption, O₂ Adsorption, H₂ Titration, and O₂ Titration on Supported Palladium Catalysts. *J. Catal.* 1999, 181, 73–79.
- (50) Pellegrini, R.; Leofanti, G.; Agostini, G.; Bertinetti, L.; Bertarione, S.; Groppo, E.; Zecchina, A.; Lamberti, C. Influence of K-doping on a Pd/SiO₂–Al₂O₃ catalyst. *J. Catal.* 2009, 267, 40–49.
- (51) Pellegrini, R.; Leofanti, G.; Agostini, G.; Rivallain, M.; Groppo, E.; Lamberti, C. Pd supported catalysts: evolution of support porous texture along Pd deposition and alkali-metal doping. *Langmuir* 2009, 25, 6476–6485.
- (52) Fagherazzi, G.; Canton, P.; Riello, P.; Pernicone, N.; Pinna, F.; Battagliarin, A. Nanostructural features of Pd/C catalysts investigated by physical methods: A reference for chemisorption analysis. *Langmuir* 2000, 16, 4539–4546.
- (53) Canton, P.; Fagherazzi, G.; Battagliarin, M.; Menegazzo, F.; Pinna, F.; Pernicone, N. Pd/CO average chemisorption stoichiometry in highly dispersed supported Pd/gamma-Al₂O₃ catalysts. *Langmuir* 2002, 18, 6530–6535.
- (54) Canton, P.; Menegazzo, F.; Polizzi, S.; Pinna, F.; Pernicone, N.; Riello, P.; Fagherazzi, G. Structure and size of poly-domain Pd nanoparticles supported on silica. *Catal. Lett.* 2003, 88, 141–146.
- (55) Montejano-Carrizales, J. M.; Aguilera-Granja, F.; Moran-Lopez, J. L. Direct enumeration of the geometrical characteristics of clusters. *Nanostruct. Mater.* 1997, 8, 269–287.
- (56) Yu, C. F.; Holby, E. F.; Yang, R. Z.; Toney, M. F.; Morgan, D.; Strasser, P. Growth Trajectories and Coarsening Mechanisms of Metal Nanoparticle Electrocatalysts. *ChemCatChem* 2012, 4, 766–770.
- (57) Campi, G.; Pifferi, A.; Mari, A.; Amenitsch, H.; Cannas, C.; Suber, L. Dynamic templating role of polynaphthalene sulphonate in the formation of silver nanocrystals in aqueous solution. *J. Nanopart. Res.* 2011, 13, 3107–3112.
- (58) Pavlopoulou, E.; Portale, G.; Christodoulakis, K. E.; Vamvakaki, M.; Bras, W.; Anastasiadis, S. H. Following the Synthesis of Metal Nanoparticles within pH-Responsive Microgel Particles by SAXS. *Macromolecules* 2010, 43, 9828–9836.
- (59) (a) Groppo, E.; Agostini, G.; Piovano, A.; Muddada, N. B.; Leofanti, G.; Pellegrini, R.; Portale, G.; Longo, A.; Lamberti, C. Effect of reduction in liquid phase on the properties and the catalytic activity of Pd/Al₂O₃ catalysts. *J. Catal.* 2012, 287, 44–54. (b) Agostini, G.; Lamberti, C.; Pellegrini, R.; Leofanti, G.; Giannici, F.; Longo, A.; Groppo, E. Effect of Pre-Reduction on the Properties and the Catalytic Activity of Pd/Carbon Catalysts: A Comparison with Pd/Al₂O₃. *ACS Catal.* 2014, 4, 187–194.
- (60) Petkov, V.; DiFrancesco, R. G.; Billinge, S. J. L.; Acharya, M.; Foley, H. C. Local structure of nanoporous carbons. *Philos. Mag. B* 1999, 79, 1519–1530.

- (61) Louca, D.; Egami, T. Local lattice distortions in $\text{La}_{1-x}\text{Sr}_x\text{MnO}_3$ studied by pulsed neutron scattering. *Phys. Rev. B* 1999, 59, 6193–6204.
- (62) Claye, A.; Fischer, J. E. Short-range order in disordered carbons: Where does the Li go? *Electrochim. Acta* 1999, 45, 107–120.
- (63) de Graaf, J.; van Dillen, A. J.; de Jong, K. P.; Koningsberger, D. C. Preparation of highly dispersed Pt particles in zeolite Y with a narrow particle size distribution: Characterization by hydrogen chemisorption, TEM, EXAFS spectroscopy, and particle modeling. *J. Catal.* 2001, 203, 307–321.
- (64) Calvin, S.; Miller, M. M.; Goswami, R.; Cheng, S. F.; Mulvaney, S. P.; Whitman, L. J.; Harris, V. G. Determination of crystallite size in a magnetic nanocomposite using extended X-ray absorption fine structure. *J. Appl. Phys.* 2003, 94, 778–783.
- (65) Baletto, F.; Ferrando, R. Structural properties of nanoclusters: Energetic, thermodynamic, and kinetic effects. *Rev. Mod. Phys.* 2005, 77, 371–423.
- (66) (a) Nemzer, S.; Harris, T.; Pister, I.; Soussan, L.; Sun, Y.; Rafailovich, M.; Frenkel, A. Size control of thiol-stabilized gold nanoparticles: Combined EXAFS and TEM characterization. *Abstr. Pap. Am. Chem. Soc.* 2005, 229, U728–U729. (b) Frenkel, A. I.; Nemzer, S.; Pister, I.; Soussan, L.; Harris, T.; Sun, Y.; Rafailovich, M. H. Size-controlled synthesis and characterization of thiol-stabilized gold nanoparticles. *J. Chem. Phys.* 2005, 123, 184701.
- (67) Guzman, C.; Del Angel, G.; Gomez, R.; Galindo, F.; Zanella, R.; Torres, G.; Angeles-Chavez, C.; Fierro, J. L. G. Gold Particle Size Determination on $\text{Au/TiO}_2\text{-CeO}_2$ Catalysts by Means of Carbon Monoxide, Hydrogen Chemisorption and Transmission Electron Microscopy. *J. Nano Res.* 2009, 5, 13–23.
- (68) Kumar, J. V.; Lingaiah, N.; Rao, K. S. R.; Ramnani, S. P.; Sabharwal, S.; Prasad, P. S. S. Investigation of palladium species in $\text{Pd/Al}_2\text{O}_3$ catalysts prepared by radiolysis method. *Catal. Commun.* 2009, 10, 1149–1152.
- (69) Narkhede, V. V.; De Toni, A.; Narkhede, V. S.; Reichinger, M.; Birkner, A.; Niemantsverdriet, J. W.; Grunert, W.; Gies, H. Pt nanoparticles inside the mesopores of $\text{TiO}_2\text{-MCM-48}$: synthesis, characterization and catalytic activity for CO oxidation. *J. Mater. Sci.* 2009, 44, 6701–6709.
- (70) Nores-Pondal, F. J.; Vilella, I. M. J.; Troiani, H.; Granada, M.; de Miquel, S. R.; Scelza, O. A.; Corti, H. R. Catalytic activity vs. size correlation in platinum catalysts of PEM fuel cells prepared on carbon black by different methods. *Int. J. Hydrogen Energy* 2009, 34, 8193–8203.
- (71) Mackay, A. L. A Dense Non-Crystallographic Packing of Equal Spheres. *Acta Crystallogr.* 1962, 15, 916.
- (72) Diebold, U. The surface science of titanium dioxide. *Surf. Sci. Rep.* 2003, 48, 53–229.
- (73) Fu, Q.; Wagner, T. Interaction of nanostructured metal overlayers with oxide surfaces. *Surf. Sci. Rep.* 2007, 62, 431–498.
- (74) Weerachawanasak, P.; Mekasuwandumrong, O.; Arai, M.; Fujita, S. I.; Praserttham, P.; Panpranot, J. Effect of strong metal-support interaction on the catalytic performance of Pd/TiO_2 in the liquidphase semi hydrogenation of phenylacetylene. *J. Catal.* 2009, 262, 199–205.
- (75) Glasner, D.; Frenkel, A. I. Geometrical Characteristics of Regular Polyhedra: Application to EXAFS Studies of Nanoclusters. *AIP Conf. Proc.* 2007, 882, 746–748. Code available on line for cluster generation of given shape and size at <http://www743.bnl.gov/frenkel/coords.html>.
- (76) Owen, E. A.; Yates, E. L. Precision measurements of crystal parameters. *Philosophical Magazine Series 7* 1933, 15 (98), 472–488.
- (77) Albers, P.; Burmeister, R.; Seibold, K.; Prescher, G.; Parker, S. F.; Ross, D. K. Investigations of palladium catalysts on different carbon supports. *J. Catal.* 1999, 181, 145–154.